Available online at www.sciencedirect.com
ScienceDirect
Geochimica et Cosmochimica Acta 71 (2007) 434–451
Geochimica
www.elsevier.com/locate/gca

Grain boundary partitioning of Ar and He

Ethan F. Baxter [a,*], Paul D. Asimow [b], Kenneth A. Farley [b]

[a] Department of Earth Sciences, Boston University, 685 Commonwealth Ave., Boston, MA 02215, USA
[b] Division of Geological and Planetary Sciences, California Institute of Technology, Pasadena, CA 91125, USA

Received 5 July 2005; accepted in revised form 12 September 2006

Abstract

An experimental procedure has been developed that permits measurement of the partitioning of Ar and He between crystal interiors and the intergranular medium (ITM) that surrounds them in synthetic melt-free polycrystalline diopside aggregates. ^{37}Ar and ^{4}He are introduced into the samples via neutron irradiation. As samples are crystallized under sub-solidus conditions from a pure diopside glass in a piston cylinder apparatus, noble gases diffusively equilibrate between the evolving crystal and intergranular reservoirs. After equilibration, ITM Ar and He is distinguished from that incorporated within the crystals by means of step heating analysis. An apparent equilibrium state (i.e., constant partitioning) is reached after about 20 h in the 1450 °C experiments. Data for longer durations show a systematic trend of decreasing ITM Ar (and He) with decreasing grain boundary (GB) interfacial area as would be predicted for partitioning controlled by the network of planar grain boundaries (as opposed to ITM gases distributed in discrete micro-bubbles or melt). These data yield values of GB-area-normalized partitioning, $\overline{K}^{Ar}_{ITM}$, with units of (Ar/m^3 of solid)/(Ar/m^2 of GB) of 6.8×10^3–2.4×10^4 m^{-1}. Combined petrographic microscope, SEM, and limited TEM observation showed no evidence that a residual glass phase or grain boundary micro-bubbles dominated the ITM, though they may represent minor components. If a nominal GB thickness (δ) is assumed, and if the density of crystals and the grain boundaries are assumed equal, then a true grain boundary partition coefficient ($K^{Ar}_{GB} = X^{Ar}_{crystals}/X^{Ar}_{GB}$), may be determined. For reasonable values of δ, K^{Ar}_{GB} is at least an order of magnitude lower than the Ar partition coefficient between diopside and melt. Helium partitioning data provide a less robust constraint with $\overline{K}^{He}_{ITM}$ between 4×10^3 and 4×10^4 cm^{-1}, similar to the Ar partitioning data. These data suggest that an ITM consisting of nominally melt free, bubble free, tight grain boundaries can constitute a significant but not infinite reservoir, and therefore bulk transport pathway, for noble gases in fine grained portions of the crust and mantle where aqueous or melt fluids are non-wetting and of very low abundance (i.e., <0.1% fluid). Heterogeneities in grain size within dry equilibrated systems will correspond to significant differences in bulk rock noble gas content.

1. Introduction

Despite the widespread use of noble gases as tracers of Earth processes and as chronometers (see McDougall and Harrison, 1999; Ozima and Podosek, 2002; Porcelli et al., 2002), many fundamental aspects of their geochemical behavior remain poorly understood. Here, we address an important characteristic of noble gas geochemistry about which no data and little understanding exist: at equilibrium, to what extent do noble gases partition between grain boundaries and crystals? This phenomenon is not commonly considered, yet if significant, it would have implications for several important fields of geochemistry, including studies of mantle evolution and noble gas-based geochronology. Partitioning, or segregation, of impurities to grain boundaries has been well documented in metals and ceramics (e.g., McLean, 1957; Sutton and Balluffi, 1995) and more recently in geological materials (e.g., Drury and Fitzgerald, 1996; de Kloe et al., 2000; Hiraga et al., 2003, 2004), but no studies have evaluated the behavior of the large, uncharged, noble gases in this regard. In practice, extrapolation of solubility or partitioning data for bulk melts to thin films or grain boundaries is not thermodynamically justified because their physical and chemical properties

* Corresponding author. Fax: +1 617 353 3290.
E-mail address: efb@bu.edu (E.F. Baxter).

0016-7037/$ - see front matter © 2006 Elsevier Inc. All rights reserved.
doi:10.1016/j.gca.2006.09.011

are fundamentally different (i.e., Rutter, 1976, 1983; Hess, 1994). Thus, independent partitioning data is desired for dry grain boundaries, which likely characterize significant portions of the lower crust and mantle.

1.1. Grain boundary partitioning: definitions

The intergranular transporting medium (herein abbreviated "ITM"; cf. Baxter and DePaolo, 2002) within a rock is of paramount importance for the transport and/or storage of material in that rock. This is because chemical transport generally occurs much more rapidly via the ITM than by volume diffusion through the solid minerals. The ITM may potentially consist of some combination of fluid phases (melts, aqueous fluids, and brines), gas phases (bubbles), and non-wetted dry grain boundaries (GB). The ITM terminology is useful in practice where the detailed phase(s) constituting the ITM is unknown, but its bulk physical–chemical properties may still be measured and modeled.

In nominally dry systems, the ITM consists only of dry grain boundaries. These grain boundaries may still constitute a significant bulk transport pathway or reservoir for an element so long as a sufficient proportion of the element is partitioned into the grain boundaries. A grain boundary, sensu stricto, is simply the interface between two crystals with differing crystallographic orientation or chemistry. The structural width of a grain boundary depends therefore on the lattice spacings of the bounding minerals (e.g., McLean, 1957). This width has been related to a single monolayer of impurities filling the mismatched crystallographic sites (e.g., Hiraga et al., 2004; Schweinfest et al., 2004) and in fact such monolayer segregations have been directly observed in some materials (e.g., Yan et al., 1998). It follows that the maximum occupancy of any impurity in a grain boundary would be equivalent to a single monolayer of that impurity. However, for trace elements (such as noble gases) that maximum occupancy may never be approached. Thus, in bulk, the effective storage capacity of the grain boundaries of such a system may be expressed as R^i_{GB}, the equilibrium ratio of the total mass of a particular element, i, stored in the grain boundaries to the total mass stored in solid crystal interiors within any volume of the system:

$$R^i_{GB} = \frac{1}{M_{s,GB}K^i_{GB}} = \frac{\phi\rho_{GB}}{K^i_{GB}(1-\phi)\rho_s}, \quad (1)$$

where $M_{s,GB}$ is the overall mass ratio between the bulk solid crystals (s) and the grain boundaries (GB), ϕ is the volume ratio of the grain boundary region to the total bulk solid (i.e., essentially GB porosity), ρ is density, and K^i_{GB} (here, $K^i_{GB} = X^i_{crystals}/X^i_{GB}$ where X is a mass fraction) represents the non-dimensional equilibrium partition coefficient (i.e., ratio of equilibrium concentrations) for the element between the solid and the grain boundary. Note that "K" is used here to represent the partition coefficient as "D" is appropriately reserved to express diffusivity.

Assuming (as we will throughout this paper) that the density of the bulk solid is similar to the density of the grain boundary region, and that $\phi \ll 1$, yields:

$$R^i_{GB} \cong \frac{\phi}{K^i_{GB}} = \frac{\hat{s}}{\overline{K}^i_{GB}}, \quad (2)$$

where $\hat{s}$ is the total grain boundary interfacial area per volume of bulk solid and $\overline{K}^i_{GB}$ (with units of [mass of element/m^3 of crystal solid]/[mass of element/m^2 of GB]) is the grain boundary area-normalized equilibrium partition coefficient for the element between solid and grain boundary. K^i_{GB} and $\overline{K}^i_{GB}$ are related to each other by the average thickness of the grain boundary region, δ:

$$K^i_{GB} = \overline{K}^i_{GB} \cdot \delta. \quad (3)$$

A reasonable estimate of $\hat{s}$ may be determined from the average grain radius, r, assuming contacting spherical grains

$$\hat{s} = \frac{4\pi \cdot r^2}{4/3\pi \cdot r^3} \cdot \frac{1}{2} = \frac{3}{2r}. \quad (4)$$

The efficiency by which the element may be transported by bulk diffusion through a grain boundary network depends on the effective bulk grain boundary diffusivity, D^*_i (cf. Baxter and DePaolo, 2002), defined as

$$D^*_i = D^i_{GB}\tau \cdot R^i_{GB} \cong \frac{D^i_{GB}\tau\phi}{K^i_{GB}} = \frac{D^i_{GB}\tau \cdot \hat{s}}{\overline{K}^i_{GB}}, \quad (5)$$

where D^i_{GB} is the molecular diffusivity of the element, i, along the grain boundary, and τ is a tortuosity factor (usually between 0.1 and 1) (cf. Brady, 1983). While estimates and/or data exist for most of these parameters, partitioning data for the noble gases is very limited, and partitioning data for nominally dry intergranular media are non-existent. The solid/ITM partition coefficient (i.e., K^i_{GB} or $\overline{K}^i_{GB}$ for an ITM with only dry non-wetted grain boundaries) is a fundamental parameter without which a full understanding of chemical transport and storage is not possible. This parameter is the target of this study.

Note that the more general term K^i_{ITM} will be used in this paper to describe the partitioning between the crystal interiors and the ITM when the nature of the ITM is unknown or unspecified. In general, $K^i_{ITM} = X^i_{xtl}/X^i_{ITM}$. In all of the above equations, "GB" may be replaced by "ITM" to describe the more general situation. Equating K^i_{GB} and K^i_{ITM} (or $\overline{K}^i_{GB}$ and $\overline{K}^i_{ITM}$) assumes the interpretation that the ITM is indeed characterized by dry grain boundaries only (i.e., without fluid or gas phases).

1.2. Importance to geochronology: understanding excess Ar (or excess He)

Ar and He are commonly used as geochronometers for igneous and metamorphic processes (e.g., McDougall and Harrison, 1999; Farley, 2002), weathering (e.g., Vasconcelos et al., 1994; Shuster et al., 2005), and extraterrestrial

processes (e.g., Turner, 1970; Culler et al., 2000; Renne, 2000). For both Ar and He thermochronometry in particular, it is commonly assumed that a "zero-concentration boundary" applies (see Baxter et al., 2002; Farley, 2002; Kelley, 2002a,b; Baxter, 2003). For this to hold it must be true either that (a) the intergranular medium is evacuated of daughter product sufficiently rapidly that the intergranular concentration remains effectively zero (i.e., short transmissive timescale, cf. Baxter, 2003), and/or (b) there is a thermodynamic preference for noble gases to be partitioned into grain boundaries, fluids or other minerals, such that the local surroundings of the mineral grain of interest behave as an infinite sink (i.e., large total local sink capacity, cf. Baxter, 2003). If these conditions do not persist while the mineral remains at least partly open to diffusion, then excess Ar or He will accumulate in that mineral, resulting in falsely old thermochronologic ages (e.g., Foland, 1979; Scaillet, 1996; Baxter et al., 2002). The transmissive timescale (τ_T) is the characteristic time required for an element, i, produced locally in a mineral of interest, j, to be transported out of the system to some external sink, located a distance L away

$$\tau^i_{j,T} = \frac{m_j L^2}{D^*_i}. \quad (6)$$

where m_j is the mode of mineral, j. Total local sink capacity (TLSC), which quantifies the equilibrium partitioning of an element (i) between a particular mineral of interest (j) and its total local surroundings, may be defined as (Baxter, 2003):

$$\mathrm{TLSC}^i_j = \frac{1}{M_{j,\mathrm{ITM}} K_{j,\mathrm{ITM}}} + \sum_k \frac{1}{M_{j,k} K_{j,k}}, \quad (7)$$

where $M_{i,x}$ and $K_{i,x}$ are the mass ratio and partition coefficient, respectively, between the mineral of interest (i) and another reservoir (i.e., another mineral (k), or the ITM) in the local system. Thus, in nominally dry systems, especially when other minerals do not act as large sinks for noble gases (i.e., when the summation term in Eq. (7) has a very small value), K^i_{GB} (or $\overline{K}^i_{GB}$) is the key parameter determining how well the grain boundaries can mediate transport and/or serve as an infinite sink and thereby prevent excess noble gases from accumulating in the mineral of interest.

1.3. Importance to noble gas transport, storage

Noble gases have been used as tracers of mantle evolution and atmosphere formation (e.g., Allegre et al., 1986; Porcelli and Wasserburg, 1995; Ozima and Podosek, 2002). It is commonly accepted that mantle melting effectively extracts noble gases from mantle solids into basaltic liquid, and many investigations have attempted to measure and apply noble gas mineral–melt partition coefficients in much the same way that, for example, lithophile ions have been studied (e.g., Hiyagon and Ozima, 1986; Broadhurst et al., 1992; Brooker et al., 2003; Parman et al., 2006). If grain boundaries are a significant thermodynamically preferred location for noble gases, then mineral–melt partitioning is not the only parameter which controls mantle degassing; instead grain boundary transport and partitioning must also be considered. Furthermore, if grain boundaries represent a significant reservoir of noble gases in the crust and mantle, then determinations of the bulk Earth noble gas budget (e.g., Dunai and Porcelli, 2002) may be affected if grain boundary noble gases are not accounted for.

2. Previous work

There have been no previous studies of noble gas partitioning in grain boundaries. However, several studies have concerned themselves with noble gas solubility and partitioning of noble gases between melts and minerals (e.g., Hiyagon and Ozima, 1986; Broadhurst et al., 1990, 1992; Carroll and Stolper, 1993; Carroll et al., 1994; Roselieb et al., 1997; Brooker et al., 1998, 2003; Chamorro et al., 2002; Kelley, 2002a; Watson and Cherniak, 2003; Parman et al., 2006). Despite this collective work, significant uncertainty remains regarding mineral solubilities and partition coefficients. Some of the earliest studies (e.g., Hiyagon and Ozima, 1986; Broadhurst et al., 1992) may have suffered from contamination of experimental mineral surfaces by glass coatings or adsorbed atmospheric gases which were not differentiated from actual lattice noble gases (see Kelley, 2002a; Brooker et al., 2003). These led to very high apparent mineral solubilities which have since been contradicted by many of the more recent studies. More recent data (reviewed in Kelley, 2002a) suggest that noble gases prefer the melt phase to the mineral lattice by several orders of magnitude although some studies (Chamorro et al., 2002) suggest that Ar solubility in melts may drop sharply at pressures above several GPa. The issue of atmospheric surface contamination as an experimental artifact remains particularly significant for Ar due to its abundance in the atmosphere, and is a major consideration in the experimental design of our experiments on grain boundaries. As described below, we get around this problem by using reactor-produced ^{37}Ar, a rare radioactive isotope that is not present in the atmosphere and thus is not susceptible to atmospheric contamination issues. While all Ar isotopes were monitored during our analysis, only ^{37}Ar was used to infer partitioning relationships between experimental reservoirs. Comparison of release patterns of ^{40}Ar vs. ^{37}Ar indicates how severe the contamination problem can be.

3. Experimental procedures

3.1. Starting material

The starting material for all experiments was a synthetic glass of near end-member diopside composition (see Table 1) which had been provided by Corning Glass to E.M. Stolper for earlier experiments. Five batches (labeled

Table 1
Starting diopside glass composition

	wt%	(2σ)[a]	Formula units[b]
SiO_2	55.73	0.54	2.001
TiO_2	0.02	0.07	0.001
Al_2O_3	0.07	0.02	0.003
Cr_2O_3	0.02	0.05	0.001
FeO	0.02	0.04	0.001
MgO	18.36	0.19	0.982
MnO	0.01	0.02	0.000
CaO	26.16	0.27	1.006
Na_2O	0.08	0.04	0.006
K_2O	0.03	0.02	0.001
Total	100.50		4.002

[a] 2σ standard deviation of 10 analyses.
[b] Normalized to six oxygens.

A–E) of 12–18 g of glass, mostly in the form of small beads, were re-melted in a Deltech furnace, in either air (A), nitrogen (B, C, and E), or argon (D) at 1 atm pressure for several hours at ~1450 °C. Glasses were rapidly quenched and examined optically to avoid bubbles. From the glass batches, cylinders ~3 mm in diameter and 5–7 mm long were cored using a diamond coring bit. Glass cores were ultrasonically cleaned in water and acetone.

3.2. Capsule preparation

Capsules were prepared to minimize the amount of air space left in the capsule during the run. Glass cylinders were fit snugly into ~3 mm ID platinum tubing. The ends of the capsules were polished down to make the glass flat and flush with the end of the platinum itself (Fig. 1a). Open-ended Pt-sleeved glass capsules were again ultrasonically cleaned in acetone after polishing. Dimensions of the polished Pt-sleeved glass cylinder were recorded. Because Pt-tubing is uniform for all experiments, the actual mass of diopside glass could be fairly accurately determined by subtracting the known weight of the measured length of Pt-tubing from the total capsule mass. At this point, all capsules (except for "pre-crystallized" experiments; see below) were sent for irradiation (see next section). Upon return from irradiation, the samples were loosely capped on both ends. Each cap was pressed out of a 1/8 in. diameter disc of platinum, and (for the most successful runs) reinforced with a second 1/8 in. disc of platinum (Fig. 1).

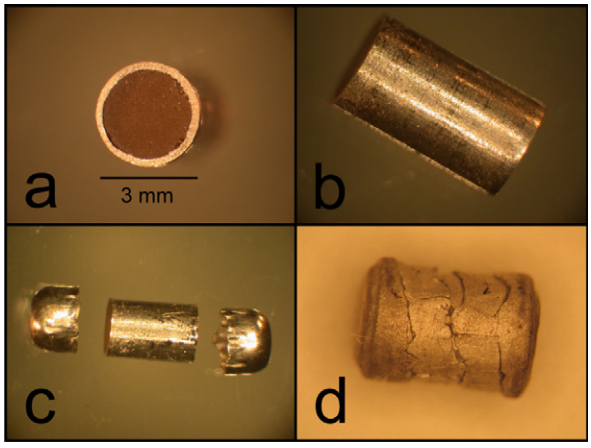

Fig. 1. Capsule design. (a) End view of platinum-walled capsule with diopside glass inside. (b) Side view of un-capped capsule before irradiation. (c) Capsule with single caps on either side about to be pressed on. (d) Double-capped capsule after piston cylinder run.

3.3. Irradiation

The purpose of irradiation is to introduce known quantities of ^{37}Ar as well as ^{4}He into the starting material. Previous work by Fechtig et al. (1960, 1961) also employed nuclear reaction production as a means of introducing noble gas isotopes into the experimental system. More recent work by Shuster and Farley (2005) has also exploited nuclear reactions to produce other noble gases in minerals for diffusion studies. The key reaction we exploit is:

$$^{40}Ca(n,\alpha)^{37}Ar$$

whereby both ^{37}Ar and ^{4}He are produced from the abundant Ca in the diopside glass. Some amount of Ne and He isotopes may also be produced from (n,α) reactions on Mg. Upon irradiation, ^{37}Ar and ^{4}He are produced within the glass structure at sites occupied by Ca and thus are homogeneously distributed throughout the glass.

In preparation for irradiation, open-ended Pt-sleeved glass cylinders were packed in aluminum discs along with loose chips of diopside glass starting material. Glass chips were used as standards for quantification of irradiation-produced ^{37}Ar and ^{4}He. Analyses of multiple glass chip standards indicated that within-disc spatial flux variations were negligible for our purposes. Packed aluminum discs were sealed in quartz glass and sent to the Oregon State Reactor Facility for irradiation in the TRIGA CLICIT (cadmium lined) reactor for 30 min. After a few weeks, samples were returned and opened at Caltech. It was noted that the diopside glass, which had originally been perfectly clear and colorless, had taken on a purplish-brown tint.

3.4. Piston cylinder experiments

After diopside glass capsules were irradiated, they were crystallized in a piston–cylinder apparatus at Caltech. The intent of this step is to allow the Ar generated within the starting glass to diffuse and distribute itself between the grain interiors and the grain boundaries at equilibrium proportions, which themselves are rapidly growing and evolving as the glass crystallizes. Conditions of piston–cylinder equilibration ranged from 1350 to 1550 °C and 2.0 to 3.0 GPa. These conditions are well below the diopside solidus, providing a melt-free system (a desired characteristic of these experiments) while allowing efficient sub-solidus crystallization. Early premelting phenomena (e.g., Lange et al., 1991) should be avoided at these conditions.

Capsules placed into the piston–cylinder assembly (MgO filler inside a graphite furnace and a CaF_2 sleeve) were not welded shut before the run. Instead, the pressure of the piston–cylinder itself "cold-welded" the capsules shut, while effectively squeezing the pore-space and air out of the capsule. If a free gas bubble remained and represented too large of a reservoir, the amount of Ar and He remaining in crystals and grain boundaries might become too small to measure accurately. To help evacuate the capsule during pressurization, a vacuum attachment was constructed which pulled a weak vacuum on the entire piston cylinder assembly during the pressurization, capsule sealing, and temperature ramp-up.

There are two kinetic issues at play during the piston–cylinder experiments. One is the rate at which noble gas may diffuse within the capsule to reach an equilibrium distribution. The second is the rate at which the glass crystallizes and coarsens (as grain boundaries develop). Nucleation and coarsening will be rapid initially, but will slow dramatically as a run proceeds. Once enough time has elapsed such that noble gas diffusion rates (constant for a given temperature) overcome grain coarsening rates, the system will have equilibrated with respect to noble gas distribution.

Piston cylinder runs were conducted for durations ranging from 1 to 180 h. After capsules were brought up to pressure under the vacuum assembly described above, temperature was increased at 100 °C/min. Sample pressure was adjusted upward as the desired temperature was approached (i.e., hot piston-in). P and T conditions were recorded at 60 s intervals during each run and were both maintained automatically throughout the run to ±5 °C, and ±50 MPa. After equilibration and sub-solidus crystallization in the piston cylinder, the sample was rapidly quenched, followed by depressurization. Contractional cracking that occurs during de-pressurization could effect the partitioning results if a significant proportion of the grain boundaries are cracked open, upon which uncharged noble gases could potentially be liberated. However, contractional cracking appears to have been limited and most grain boundaries remain intact so this effect is negligible (see Sections 5.4.1 and 5.5).

3.5. Pre-crystallized experiments

Two additional samples were prepared with a modified method to serve as a standard of sorts in differentiating noble gases stored in crystals from those stored in grain boundaries. These "pre-crystallized" samples were prepared identically to those described above except that the diopside starting glass was sealed and crystallized in the piston cylinder *before* being sent for irradiation (pre-crystallized samples were run at 1450 °C and 1.0 GPa for 20 h). Because the diopside crystals (as opposed to the grain boundary region) make up ~99.99% of the total mass fraction of a crystallized sample (and include, therefore, ~99.99% of the Ca), the *in situ* produced noble gases would also reside 99.99% within the crystals. Upon return from irradiation, pre-crystallized samples were *not* subsequently re-equilibrated in the piston cylinder. Instead they were immediately analyzed for noble gases as described in Section 4 below. The characteristics of noble gas release from these pre-crystallized samples provide the signature of noble gases stored exclusively within the crystals.

4. Noble gas analysis

The Caltech noble gas laboratory includes a preparation line with a resistance furnace front end as well as portals where other sample introduction apparatus may be attached. The preparation line allows for the concentration of pure He and Ar from the same sample for introduction into one of three spectrometers. Helium was analyzed on a MAP gas source mass spectrometer dedicated to Helium analysis. For the first year of analysis (until and including April 2002), Ar was analyzed on a second gas source mass spectrometer. For the second year of analyses (comprising the majority of the successful experiments) Ar was analyzed on a Balzers Prisma quadrupole mass spectrometer. Air calibrations and blanks were run regularly to monitor and correct for instrument drift, multiplier gain, and sensitivity. ^{37}Ar blanks on the gas source mass spectrometer were $<0.001 \times 10^{-9}$ cm^3 STP. ^{37}Ar blanks on the quadrupole mass spectrometer were $<0.01 \times 10^{-9}$ cm^3. Based on the reproducibility of air standards over the duration of the analyses, Ar and He abundance measurements have a ~7% uncertainty.

4.1. Capsule piercing

Sample capsules were individually pierced by lowering a screw-driven blunt tipped conical piercer into the capsules. Typically, the piercer was driven more than half way through the capsule, rupturing it and in many cases literally tearing it about its middle. All gas released during this pierce was collected and analyzed. After pierce, samples were heated in the piercing chamber to ~150 °C using a heat gun and monitored by a contacting thermocouple. Gas released during this heating was collected and analyzed. For a few early samples, a second pierce (i.e., a retraction and deeper plunge of the piercer) and/or a second low temperature heating (i.e., after cool down, a second ~150 °C heating) was performed to see if additional gas was released. Each of these experiments revealed insignificant additional gas release upon a second prolonged pierce/heating, so further samples were pierced and heated at ~150 °C only once each.

4.2. Capsule preparation for furnace heating and thin sections

Next, samples were removed from the piercer chamber. Each sample examined at this point had clearly been breached if not nearly torn in half by the piercer. Any gas

trapped within bubbles inside the capsule should have been liberated during the pierce. At this point, many of the samples were divided into a portion for thin section preparation, and the remainder for furnace step heating. For the furnace samples, platinum capsule walls were removed and a fraction of the remaining diopside aggregate was weighed and prepared for furnace loading. This fraction comprised mostly large cohesive aggregates with a smaller amount of finer grained debris from the piercing. Other capsules for which thin sections were not prepared were loaded in their entirety (including platinum) for furnace heating.

4.3. Step heating analysis

Samples for furnace heating were wrapped in high purity tin foil balls. Each sample was dropped into the cold furnace individually before step heating analysis proceeded. Furnace temperatures were monitored with a pyrometer for temperatures above about 900 °C and by electrical current settings determined by thermocouple calibration for lower temperatures. Thus, the uncertainty of furnace interior temperatures below 900 °C is less robust (±50 °C) than at high temperatures (±10 °C). However, when several furnace runs were performed in sequence, the furnace window (through which the pyrometer reads black-body radiation temperature) becomes clouded and temperature measurements are impaired. Thus, each set of four or five consecutive furnace samples were calibrated based on electrical current settings and pyrometer readings from when the window was clean. Overall, we consider ±50 °C as the uncertainty in all furnace temperatures.

For each temperature in the step heating analysis, desired temperatures were maintained for 15 min and the gas released during that time collected for analysis. Between each temperature step, the power was cut and the furnace allowed to cool to 300 °C or lower before the ramp up to the next temperature began. The final temperature step for all analyses was >1450 °C, sufficient to melt diopside and release any remaining bound gas. Many samples were followed up by a re-extract at the fusion temperature which always yielded insignificant additional gas release.

The net result of the noble gas analysis is a step heating release profile for each sample. By summing the noble gases released in all steps (including piercer chamber), accounting for the mass of the furnace sample fraction and the radioactive decay of ^{37}Ar, and comparing to irradiated pure glass standards, a total noble gas yield for each sample was calculated. A 100% yield means that all noble gas known to have been produced during irradiation in the starting material was accounted for in the total measurement. Step heat release profiles for each sample were compared to the step heat release profile for the pre-crystallized samples. All noble gases released at temperatures which showed no release from the pre-crystallized samples must be derived from somewhere other than the crystal interiors. Only four other possible reservoirs exist in the samples: (1) gas bubbles, (2) un-crystallized pockets of glass, (3) platinum–diopside phase boundaries, (4) diopside–diopside grain boundaries. Gases in bubbles are easily distinguished as they would be released during piercing (though see Section 5.5.1). Gases in un-crystallized glass should be negligible as the aim of the piston cylinder experiment design was to crystallize the samples 100% (evaluated by thin sections; see Section 5). Gases along the boundary between the platinum capsule and the diopside crystals should be negligible given the insignificant proportion of those phase boundaries. The most likely (and desired) reservoirs are the diopside–diopside grain boundaries within the sample. This assumption can be tested by comparing gas release patterns from capsules of different piston cylinder crystallization duration (and hence grain size, and total grain boundary surface area).

5. Results

5.1. General

A total of 48 samples were run in the piston cylinder. The first half of these (EB001–EB025) were exploratory in nature and were used mainly to perfect the sample preparation and sealing protocols as well as to develop an appropriate step-heating schedule. Successful samples consistently produced ^{37}Ar yields of 80% or better, and ^{4}He yields of 50% or better; all such samples were included in the final data interpretations and are described in Table 2. This apparent gas loss could be due to, (1) measurement uncertainty in mass of original glass for each sample; (2) analytical uncertainty in samples and standards, magnified in some cases by the ^{37}Ar decay correction; (3) leakage from capsules before they were totally sealed within the piston cylinder; (4) diffusional loss of gas through the platinum walls at high temperature; (5) loss of gas due to inadvertent disaggregation and handling between piercing and furnace analysis (see Section 5.4.1). Only option #5 above could potentially skew our final interpretations (for example, if the gas lost during handling was mostly from grain boundaries). In any case, the missing amount is small enough to have minimal effects on our ultimate calculations of grain boundary partitioning. These effects can be assessed by adding the "missing" noble gas back into each sample as grain boundary gas (see Section 5.4.3).

5.2. Standards

Analysis of standard diopside glass shards shows that the irradiation produced 0.09×10^{-9} cm^3 STP ^{37}Ar per mg of diopside after 30 min of irradiation in the CLICIT reactor facility at Oregon State University. ^{4}He was produced at 0.26×10^{-9} cm^3 STP per mg of diopside per 30 min of irradiation, suggesting that much ^{4}He (about 0.17×10^{-9} cm^3 STP) was produced by α-producing reactions other than the ^{40}Ca$(n,\alpha)^{37}$Ar reaction (such as ^{24}Mg$(n,\alpha)^{21}$Ne). In the case of ^{37}Ar, which has a radioac-

Table 2
Sample information

Piston cylinder run information										Noble gas analysis information			
Capsule	Irradiation date	Piston–cylinder start date	Starting glass batch[a]	Total diopside mass (mg)	Max P (GPa)	Max T (C)	Run duration at P–T (h)	Thin section?	$\hat{s}$ (m^2/m^3)[b]	Ar, He Analysis start date	Pierce?	Step heat?	Diospide mass of furnace fraction (mg)
EB027	9/24/2001	5/23/2002	C	114.2	2.0	1450	70	y	4.3×10^4	na	n	n	na
EB028	9/24/2001	3/18/2002	C	106.6	2.0	1450	20	n	8.9×10^4	3/25/2002	y	y	106.6
EB029	9/24/2001	4/2/2002	C	108.7	2.0	1450	20	n	8.9×10^4	4/18/2002	y	y	108.7
EB030	9/24/2001	4/4/2002	C	99.1	2.0	1450	20	n	8.9×10^4	4/18/2002	y	y	99.1
EB031	9/24/2001	4/8/2002	C	108.9	2.0	1450	70	n	4.6×10^4	4/18/2002	y	y	108.9
EB032	4/19/2002	5/6/2002	C	102.6	2.0	1450	16	y	1.0×10^5	na	n	n	na
EB033	4/19/2002	5/7/2002	C	103.2	2.0	1450	8	n	1.4×10^5	5/22/2002	y	y	103.2
EB034	4/19/2002	5/7/2002	C	103.6	2.0	1440	12	n	1.1×10^5	5/22/2002	y	y	103.6
EB035	4/19/2002	5/10/2002	C	89.5	2.0	1450	70	n	4.6×10^4	5/22/2002	y	y	89.5
EB036	4/19/2002	6/7/2002	C	110.7	2.0	1450	70	y	4.8×10^4	6/11/2002	y	y	22.4
EB037	4/19/2002	6/5/2002	C	90.5	2.0	1450	20	y	7.9×10^4	6/11/2002	y	y	31.4
EB038	4/19/2002	6/27/2002	C	95.9	2.0	1450	8	n	1.4×10^5	7/18/2002	y	y	95.9
EB040	4/19/2002	6/28/2002	D	114.5	2.0	1450	8	y	2.9×10^5	7/18/2002	y	y	52.9
EB044	4/19/2002	8/6/2002	D	113	2.0	1450	180	y	5.5×10^4	9/11/2002	y	y	56.8
EB048	4/19/2002	8/29/2002	D	116.6	3.0	1550	134	y	6.6×10^4	9/11/2002	y	y	43.5
EB049	4/19/2002	6/6/2002	E	110.9	2.0	1450	2	y	1.7×10^5	6/11/2002	y	y	16.6
EB050	4/19/2002	7/21/2002	E	109.4	2.0	1450	180	y	3.3×10^4	7/30/2002	y	y	30.4
EB051	4/19/2002	6/26/2002	E	98.4	<2.0	?	fail	n	na	na	n	n	na
EB052	4/19/2002	7/9/2002	E	114.1	3.0	1550	9	y	6.7×10^4	7/19/2002	y	y	31.5
EB053	4/19/2002	7/10/2002	E	98.6	2.0	1350	20.5	y	1.6×10^5	7/19/2002	y	y	38.3
EB054	4/19/2002	7/10/2002	E	91.8	2.0	900	fail	n	na	na	n	n	na
EB058	6/17/2002	5/20/2002	C	89.9	2.0	1450	20 (pre-xtl)	n	na	7/18/2002	y	y	na
EB059	6/17/2002	6/4/2002	E	101.6	2.0	1450	20 (pre-xtl)	y	na	8/4/2002	y	y	na

Note. Skipped capsule numbers in sequence indicate diopside glass cylinders that were cut, but never used.

[a] See text Section 3.1.

[b] Determined from thin sections and see Eq. (4).

tive half-life of 34.95 days (Renne and Norman, 2001), these measurements had to be decay corrected for purposes of inter-comparison. We also detected ^{3}He in our irradiated glass standards (and samples) in amounts that increased with time. Our hypothesis regarding the ^{3}He is that a small amount of tritium was produced from trace Lithium in our starting glass. Tritium decay to ^{3}He would account for the increasing levels of ^{3}He with time after irradiation. Accounting for ^{3}He in-growth, ^{3}He release patterns from our samples are the same as ^{4}He release patterns, so we report only the latter.

5.3. Pre-crystallized experiments

Table 3 and Fig. 2 show step release data for these samples (EB058 and EB059). Both show significant release of Ar only upon high temperature fusion with essentially zero release of Ar at all lower temperature steps and piercing. Thus, in the equilibrated experiments discussed below, any ^{37}Ar released at lower temperature steps must derive from a reservoir in the sample other than the crystal interiors (i.e., the ITM). For He, the step release data for pre-crystallized samples shows that He in the crystal interiors is released at the 750 °C temperature step and above. In using the step release pattern of pre-crystallized samples to identify the crystal interior noble gases released from the equilibrated samples, we assume that the noble gases in these two types of experiment are sited similarly within the crystals, and therefore have similar retentivity (see electronic annex EA-1 for discussion).

5.4. Equilibrated samples

Seventeen successfully equilibrated and fully analyzed samples (EB028–EB053) were produced (Table 2). Step release data are shown in Table 4a, 4b,4c for ^{37}Ar, ^{40}Ar, and ^{4}He. ^{37}Ar release data are shown in terms of the percent of total ^{37}Ar expected, based on the standard glasses and age corrections. Here, the large effect of atmospheric contamination on the ^{40}Ar is illuminated. The ^{40}Ar data always include a large release at the 400 °C step, as opposed to ^{37}Ar for which there is essentially zero release at 400 °C. Hence, the Ar released at the first furnace heating step consists

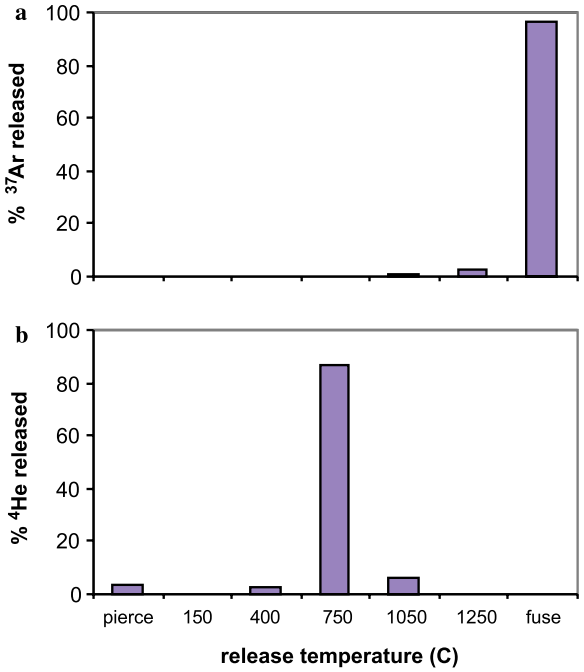

Fig. 2. Representative pre-crystallized experiment (EB058). (a) ^{37}Ar is released from grain interiors only upon fusion. (b) ^{4}He is released from grain interiors mostly at 750 °C and above.

mostly of atmospheric ^{40}Ar adsorbed onto the sample surfaces during transfer from the piercing chamber and preparation for furnace analysis. Had ^{40}Ar been used to measure Ar partitioning within the sample, gross errors would have resulted due to this atmospheric contamination effect. Note also that as the adsorbed atmospheric ^{40}Ar is burned off, higher temperature release patterns of ^{40}Ar match more closely those for ^{37}Ar.

5.4.1. Sample yields

All but one of the 17 successfully sealed and fully analyzed samples produced ^{37}Ar yields between 80% and 104%. Sample EB048 produced an apparent total sample yield of 129%. While it is not clear exactly what has caused this high yield, the relative amounts of noble gas released from this mass fraction during step heating are still useful. Thus, sample EB048 is included in final interpretations and analysis.

Table 3
Noble gas release data for pre-crystallized samples

Sample	Total diospide mass (mg)	Diopside mass of furnace fraction (mg)	Pierce	150 °C	400 °C	750 °C	1050 °C	1250 °C	Fuse	Yield
% of total ^{37} Ar in sample (decay and blank corrected)										
EB058	89.9	89.9	0.1	0	0.1	0.3	0.7	2.2	89.9	93.3
EB059	101.6	52.0	na	na	0.2	0.2	0.9	1.9	97.9	101.1
×10 $^{-9}$ cm^3 STP ^{40}Ar/mg released in each 20 min step (blank corrected)										
EB058	89.9	89.9	0.840	0.163	1.253	0.679	0.664	0.219	0.790	na
EB059	101.6	52.0	na	na	3.341	0.761	0.910	0.157	0.384	na
×10 $^{-9}$ cm^3 STP ^{4}He/mg released in each 20 min step (blank corrected)										
EB058	89.9	89.9	0.0086	0.0009	0.0061	0.2124	0.0157	0.0010	0.0005	92.7
EB059	101.6	52.0	na	na	0.0158	0.2360	0.0218	0.0000	0.0000	103.5

Table 4a
^{37}Ar step heating data

Sample	Pierce	150	Crush	400	750	1050	1250	Fuse	Yield%	R_{GB}	$\overline{K}^{Ar}_{ITM}$	$\overline{K}^{Ar}_{ITM}$ leak corrected
% of total ^{37}Ar in sample (decay and blank corrected)												
Samples with thin section												
EB036	17.7	0.4	na	1.4	20.4	19.5	17.2	13.3	90	4.4	1.1×10^{4}	9.3×10^{3}
EB037	14.9	0.4	na	1.3	33.9	16.1	11.3	20.5	98	3.1	2.6×10^{4}	2.5×10^{4}
EB040	1.4	0.1	na	0.5	4.3	21.8	4.2	59.9	92	0.5	5.5×10^{5}	4.4×10^{5}
EB044	4.6	1.5	na	1.5	10.2	21	23.4	17.4	80	3.3	1.7×10^{4}	1.2×10^{4}
EB048	30.5	0.2	na	2.9	21.5	55.5	8.9	9.2	129	9.7	6.8×10^{3}	na
EB049	12.6	0.6	na	0.9	49.2	5.4	2.6	19.2	91	3.1	5.6×10^{4}	4.8×10^{4}
EB050	82.2	0	na	1	4.5	3.2	3.5	8.8	103	1.4	2.4×10^{4}	na
EB052	18.2	0.2	na	1	11.7	52.9	6.1	13.8	104	5.2	1.3×10^{4}	na
EB053	80.6	1.3	na	0	1.2	0.6	0	1.6	85	1.9	8.2×10^{4}	1.4×10^{4}
Samples without thin section												
EB028	41.1	3.3	na	0.5	17.7	7.1	3.8	11.6	85	2.8	3.2×10^{4}	2.2×10^{4}
EB029	31.3	0.3	na	0.3	20.9	18.6	5.6	5.9	83	7.7	1.1×10^{4}	8.4×10^{3}
EB030	35.6	1	2.5	0	9.1	11.3	4.3	20.8	85	1.4	7.2×10^{4}	4.2×10^{4}
EB031	22.3	1.2	na	0.6	19.7	22.7	4.6	13.9	85	3.5	1.3×10^{4}	9.9×10^{3}
EB033	55.4	4.9	na	0.3	7	4	3.2	16.7	92	1.2	1.2×10^{5}	8.2×10^{4}
EB034	18.8	0.7	na	0.3	24.1	6.5	5.4	39.8	96	0.9	1.2×10^{5}	1.1×10^{5}
EB035	14.4	0.5	na	0.1	25.8	29	12.1	16.8	99	4.0	1.1×10^{4}	1.1×10^{4}
EB038	3	0.2	na	0.4	9.4	32.4	3.8	40.5	90	1.1	1.2×10^{5}	9.8×10^{4}

Note. Samples had 0.09×10^{-9} cm^3 STP ^{37}Ar/mg at time of irradiation. Note. Furnace blanks (i.e., background levels) were less than 0.01×10^{-9} cm^3 STP ^{37}Ar.

Table 4b
^{40}Ar Step Heating Data

Sample	Pierce	150	Crush	400	750	1050	1250	Fuse
$\times10^{-9}$ cm^3 STP ^{40}Ar/mg released in each 20 min step (blank corrected)								
Samples with thin section								
EB036	0.202	0.185	na	18.343	2.775	0.072	0.482	0.059
EB037	0.109	0.066	na	5.342	0.604	0.237	0.162	0.268
EB040	0.394	0.109	na	1.581	1.489	5.983	1.195	15.281
EB044	0.733	0.388	na	2.602	1.806	3.242	3.582	2.646
EB048	4.788	0.081	na	2.398	3.176	6.654	0.929	1.027
EB049	0.306	0.158	na	5.465	2.184	0.000	0.000	0.418
EB050	1.073	na	na	4.787	1.521	0.033	0.038	0.133
EB052	0.480	0.080	na	7.276	2.159	1.375	0.142	0.398
EB053	1.434	0.079	na	na	4.014	0.044	na	0.039
Samples without thin section								
EB028	1.126	0.237	na	1.452	0.776	0.131	0.000	0.230
EB029	1.700	0.150	na	1.260	1.680	1.240	0.440	0.390
EB030	0.880	0.570	0.027	na	2.500	0.350	0.083	0.380
EB031	0.430	0.100	na	1.500	0.350	0.170	0.017	0.053
EB033	0.596	0.118	na	0.557	0.241	0.129	0.212	0.362
EB034	0.292	0.059	na	1.961	0.803	0.084	0.242	0.547
EB035	0.209	0.161	na	0.617	0.426	0.363	0.086	0.137
EB038	0.098	0.173	na	1.756	0.564	0.501	0.202	0.593

Note. Furnace blanks range from 2 to 15×10^{-9} cm^3 STP total.

As described above, for many samples only a fraction of diopside (between 10% and 50% of the entire diopside mass) was recovered after piercing and placed into the furnace for step heating (Table 2). An important assumption regarding the interpretation of such samples is that the distribution of noble gases throughout each sample is homogeneous such that the split placed in the furnace (and its noble gas release characteristics) is representative of the whole. Several tests confirm this to be a robust assumption, though we found that intentional or inadvertent disaggregation of the sample between pierce and furnace analysis can result in some loss of grain boundary noble gases (see electronic annex EA-2). This might be more alarming if we were interested in measuring charged species (e.g., cations); but because noble gases are uncharged it is not unreasonable that they would be freed from grain bound-

Table 4c
^{4}He step heating data

Sample	Pierce	150	Crush	400	750	1050	1250	Fuse	Yield%	R_{GB}	$\overline{K}^{He}_{ITM}$	$\overline{K}^{He}_{ITM}$ leak corrected
$\times 10^{-9}$ cm^3 STP ^{4}He/mg released in each 20 min step (blank corrected)												
Samples with thin section												
EB036	0.0759	0.0109	0.0000	0.1124	0.0056	0.0000	0.0000	0.0075	80	9.4	5.1×10^3	3.6×10^3
EB037	0.0712	0.0164	0.0000	0.1444	0.0027	0.0000	0.0000	0.0000	89	60.1	1.3×10^3	1.1×10^3
EB040	0.0112	0.0245	0.0000	0.0627	0.1099	0.0378	0.0060	0.0017	96	0.6	5.1×10^5	4.5×10^5
EB044	0.0066	0.0095	0.0000	0.0881	0.0344	0.0000	0.0000	0.0000	52	2.8	2.0×10^4	8.5×10^3
EB048	0.0531	0.0114	0.0000	0.0526	0.0136	0.0051	0.0000	0.0000	51	3.4	1.9×10^4	6.4×10^3
EB049	0.0472	0.0392	0.0000	0.0605	0.0378	0.0000	0.0000	0.0000	70	2.6	6.4×10^4	3.6×10^4
EB050	0.2189	0.0017	0.0000	0.0194	0.0045	0.0090	0.0075	0.0000	99	1.0	3.3×10^4	2.8×10^4
EB052	0.0626	0.0545	0.0000	0.1401	0.0087	0.0043	0.0000	0.0014	103	13.5	4.9×10^3	na
EB053	0.2340	0.0039	0.0000	0.0000	0.0071	0.0059	0.0000	0.0000	95	0.3	5.4×10^5	1.2×10^5
Samples without thin section												
EB028	0.1175	0.0293	0.0000	0.0578	0.0252	0.0074	0.0017	0.0006	91	2.5	3.6×10^4	2.8×10^4
EB029	0.1402	0.0073	0.0000	0.0593	0.0473	0.0052	0.0009	0.0004	99	1.2	7.2×10^4	6.8×10^4
EB030	0.0704	0.0075	0.0105	0.0296	0.0972	0.0164	0.0030	0.0015	89	0.4	2.2×10^5	1.4×10^5
EB031	0.0625	0.0082	0.0000	0.1336	0.0250	0.0091	0.0012	0.0008	91	3.9	1.2×10^4	1.0×10^4
EB033	0.1556	0.0135	0.0000	0.0121	0.0274	0.0074	0.0045	0.0012	84	0.6	2.2×10^5	8.1×10^4
EB034	0.0574	0.0242	0.0000	0.0878	0.0542	0.0106	0.0060	0.0000	91	1.6	7.2×10^4	5.9×10^4
EB035	0.0653	0.0090	0.0000	0.1233	0.0363	0.0045	0.0000	0.0000	90	3.2	1.4×10^4	1.2×10^4
EB038	0.0179	0.0410	0.0000	0.0957	0.0602	0.0147	0.0057	0.0009	89	1.7	8.2×10^4	6.8×10^4

Note. Furnace blanks were less than 0.1×10^{-9} cm^3 ^{4}He.

aries when grains were separated during disaggregation. Therefore, large coherent chunks from all samples for which thin sections were made were selected for the step heating analysis to minimize this loss. Some amount of disaggregation is unavoidable so it is possible that noble gas loss from the grain boundary region in samples due to this effect may contribute somewhat to sub-100% yields.

5.4.2. Intragrain melt or fluid inclusions

We interpret the gas released at fusion as atoms residing within the structure of crystal interiors, however, there is the possibility that some of it resides in melt or fluid inclusions too small to be accessed during step-heating. In this case, the reported partition coefficients would be upper limits. We sought an impurity-poor starting material that would crystallize completely to a monomineralic assemblage in order to minimize this problem, but it is difficult to exclude it completely; concentration of any impurities into low-degree residual melts could lead to a composition with liquidus temperature below the temperature of our experiments. However, exhaustive search of three experimental thin sections shows such inclusions to be absent or extremely rare in well-crystallized runs; in fact only one or two small (<3 μm) melt inclusion candidates were identified in total. If these are melt inclusions, we can assume the crystal/melt partition coefficient is of order 10^{-4} (Chamorro et al., 2002). In order for melt inclusions to hold a significant amount of Ar, the volume fraction of melt would have to exceed 10^{-4}. Our observations suggest a volume fraction of about 10^{-6} (i.e., one 3 μm inclusion in a 3 mm diameter thin section). Unless the thin sections examined are atypical or there are significant inclusions too small to resolve optically and yet too rare to be found by SEM and TEM imaging, we conclude that inclusions are a negligible issue.

5.4.3. Differentiating grain boundary noble gases with the grain size correlation

Any gas released at lower temperature steps (temperatures below fusion for Ar; $T < 750$ °C for He) should include gas that had been sited in the grain boundaries. If we can identify the grain boundary gases from those steps we can calculate R^i_{GB} [Eqs. (1) and (2)] for each sample. There should be a positive correlation between the total amount of grain boundary noble gases and the total grain boundary surface area (inversely related to grain size) so long as a constant equilibrium partitioning of noble gases between grain boundaries and crystal interiors has been reached. Grain size is controlled by varying run duration (longer runs produce larger grains). Grain boundary surface area ($\hat{s}$) for each sample (Table 2) was measured directly from thin sections using the grain boundary line intercept method of Smith and Guttman (1953) and Mendelson (1969). For samples without thin sections, $\hat{s}$ was based on the average of grain sizes observed in other runs (including many early runs not listed in Table 2) of like duration and conditions.

Fig. 3 shows the percent of ^{37}Ar released at pierce versus $\hat{s}$. There is no correlation between pierce released gas and grain boundary surface area. This argues against the possibility that the pierce releases gas that resided in grain boundaries during the experiment. More likely, this gas represents that which was actually in a free vapor bubble during the experiment, the exact quantity of which depends on how well the capsule was evacuated before sealing in the piston cylinder. Those that were evacuated more fully had

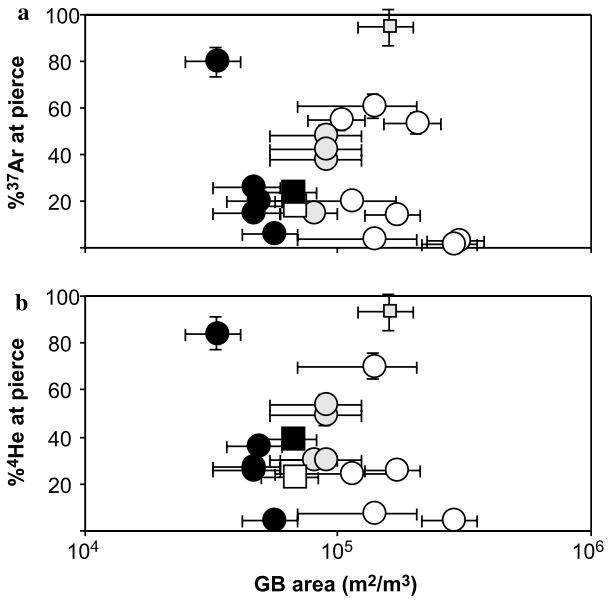

Fig. 3. Bulk noble gas released at capsule pierce as a function of grain boundary surface area. Neither ^{37}Ar (a) nor ^{4}He (b) show any trend. Circles are 1450 °C runs. Large squares are 1550 °C runs. Small square is the 1350 °C run. White = <20 h run, gray = 20–20.5 h run, black = >20.5 h run.

very little initial gas (i.e., air) in them and thus a smaller free gas phase into which ^{37}Ar could then partition, yielding smaller gas release at pierce. The story is similar for He.

Fig. 4 shows the percent of gas from lower temperature steps (including pierce) vs. $\hat{s}$. This plot also shows no discernible correlation for ^{37}Ar or ^{4}He. For these reasons, we interpret gas released upon capsule piercing as gas residing within free gas bubbles of varying size. Pierce released gas will not be considered in calculating grain boundary partitioning.

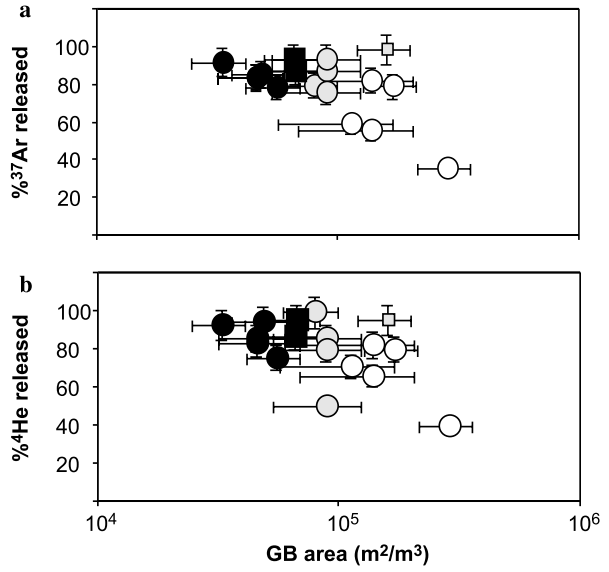

Fig. 4. Bulk noble gas released at all low-temperature steps, including pierce (i.e., not including release at fusion). Though the eye is drawn to the single low release data point, discounting that, neither ^{37}Ar (a) nor ^{4}He (b) show any meaningful trend. Symbols are as in Fig. 3.

5.4.4. Approach to equilibrium

Fig. 5a shows the ^{37}Ar data plotted as R_{GB}^{Ar} (as in Table 4a; the ratio of hypothesized grain boundary ^{37}Ar [150–1250 °C release] to crystal interior ^{37}Ar [>1450 °C release]) versus GB area. Fig. 6a shows the ^{4}He data plotted as R_{GB}^{He} (as in Table 4c; the ratio of 150–400 °C release to >750 °C release). Recall from Eq. (2) the expected relationship between these parameters (R_{GB}^{i} and $\hat{s}$) from which $\overline{K}_{GB}^{i}$ may be determined. To consider the possible effects of grain boundary noble gas loss during transfer and preparation of samples for furnace analysis, Figs. 5b and 6b include "missing" noble gases calculated from sub-100% yields in the inferred grain boundary fraction. For samples with 100% (or greater) apparent yield, the resulting values in this plot are identical to those in Figs. 5a and 6a. These plots thus assume that sub-100% noble gas yields are due entirely to post-pierce loss of grain boundary noble gases.

At first glance, the predicted correlation seems to be lacking in Figs. 5 and 6. In particular, the shortest duration runs (with the greatest GB area) appear to have far too little in their grain boundaries compared to longer duration runs.

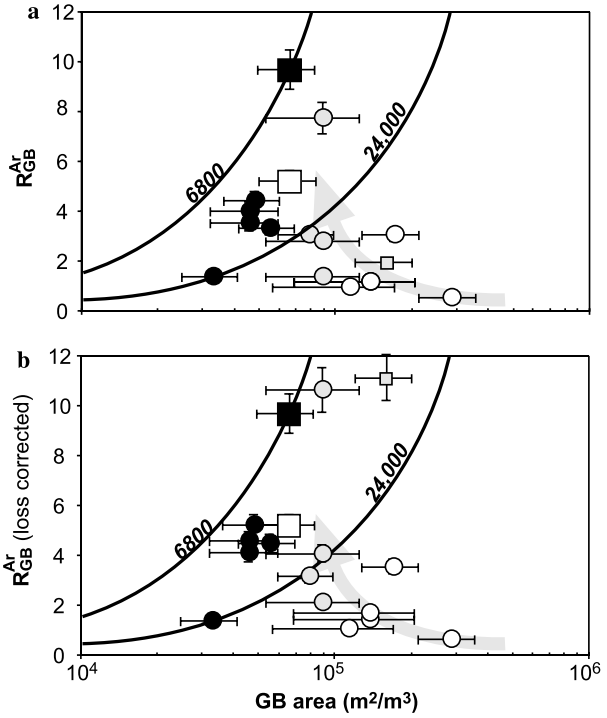

Fig. 5. Ratio of inferred grain boundary ^{37}Ar to crystal interior ^{37}Ar (R_{GB}^{Ar}), plotted against grain boundary area ($\hat{s}$). Symbols are as in Fig. 3. (a) Grain boundary argon is assumed to be represented by release at all temperatures from 150 to 1250 °C. (b) Argon lost from the capsule is added back in as grain boundary argon. Lines of constant $\overline{K}_{ITM}^{Ar}$ are shown which bound all presumed equilibrium data of >20 h duration (all black symbols and some gray, near equilibrium, symbols). These equilibrium data show the expected trend of decreasing grain boundary argon with decreasing grain boundary surface area. Gray arrow indicates the inferred path towards equilibrium partitioning as indicated by <20 h experiments.

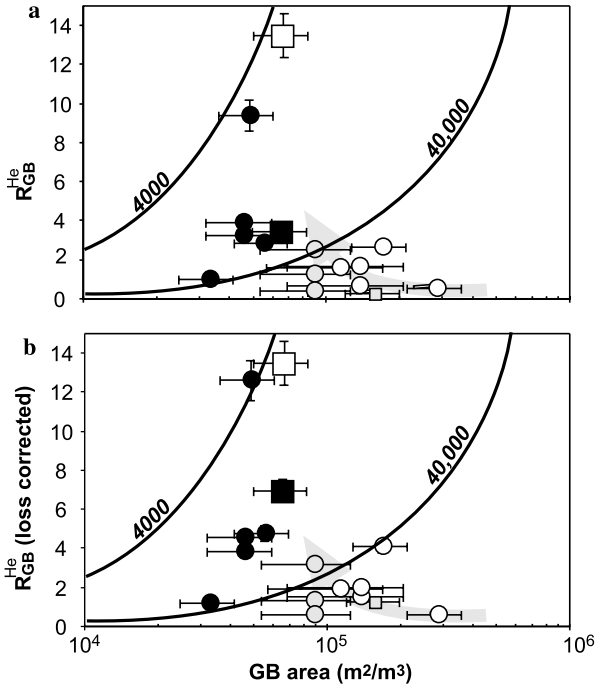

Fig. 6. Ratio of grain boundary ^{4}He to crystal interior ^{4}He (R^{He}_{GB}), plotted against grain boundary area ($\hat{s}$). Symbols are as in Fig. 3. (a) Grain boundary He is assumed to be represented by release at all temperatures from 150 to 400 °C. (b) He lost from the capsule is added back in as grain boundary He. Lines of constant $\overline{K}^{He}_{ITM}$ are shown, which bracket the equilibrium data. Gray arrow indicates the inferred path towards equilibrium partitioning as indicated by <20 h experiments.

Also note that the four 20 h replicates yield a very large spread. The poor reproducibility of the 20 h replicates may indicate a transition in the system from short runs (<20 h) that failed to reach a fixed equilibrium to longer runs (>20 h) where equilibrium partitioning was attained. Equilibration is limited by the competition between noble gas diffusion and grain coarsening which, during early stages, will be incorporating gases into rapidly coarsening crystals faster than they can diffuse out to a decreasing proportion of grain boundaries. This transition to equilibrium is supported by looking only at the longer duration runs where a more systematic trend of decreasing R^i_{GB} with decreasing grain boundary surface area is displayed. The excellent reproducibility of the three 70 h replicates is another indication that equilibrium has been achieved. Of the two runs at 1550 °C, EB048 (134 h) certainly also reached equilibrium. With only one run at 1350 °C (EB053) for only 20.5 h it is possible that this sample did not reach equilibrium. It would have been desirable to add even coarser grained samples to the dataset. But, due to the exponential decrease in grain coarsening rate (compare Fig. 7c and d), we were unsuccessful in producing coarser run products.

An alternative explanation for the increasing fraction of low-temperature release gas in the finer grained (i.e., <20 h) runs might be that this release is promoted by cracking open of grain boundaries due to thermal stresses during step-heating, whose magnitude increases with increasing grain size. This is possible, but this effect should continue to grow worse with increasing grain size in the longer runs, where we see the opposite trend, i.e., apparent equilibrium partitioning with decreasing fraction of low-temperature release as grain boundary area decreases. We conclude that grain-size correlated thermal cracking during step heating is not the main mechanism for release of GB-bound atoms in the longer runs.

Contours of constant $\overline{K}^i_{ITM}$ that bracket all the >20 h equilibrium data (including some of the 20 h runs which perhaps did just reach equilibrium) are shown in Figs. 5 and 6. These combined data suggest an overall constraint on $\overline{K}^{Ar}_{ITM}$ of 6.8×10^3–2.4×10^4 m^{-1}. Helium data reveal a similar, though more poorly constrained, trend. Considering >20 h runs, the data suggest a constraint on $\overline{K}^{He}_{ITM}$ of 4×10^3–4×10^4 m^{-1}. A slight trend towards lower $\overline{K}^{Ar}_{ITM}$ (and $\overline{K}^{He}_{ITM}$) with increasing temperature is evident (see discussion in electronic annex EA-3). It is interesting that the grain boundary partition coefficients of He and Ar are essentially equal for the long duration 1450 and 1550 °C experiments where we can confidently conclude that equilibrium has been reached.

5.5. Characteristics of the grain boundary region

The above analysis of release spectra and grain size leads to a robust constraint on $\overline{K}^i_{ITM}$. Now, in order to convert $\overline{K}^i_{ITM}$ (with units of m^{-1}) into a true partition coefficient, K^i_{ITM} [see Eq. (3)], we must assess or assume the characteristics of the ITM region. In particular, we need to know if the ITM was indeed melt free and, if so, to constrain the average width of the grain boundary region, δ. We attempted to constrain the ITM characteristics by four methods: petrographic light microscope, TEM, SEM, and previously published literature on grain boundaries in general. Representative thin sections are shown in Fig. 7a–d. See electronic annex EA-4 for discussion of SEM and TEM analyses.

Overall, most grain boundaries and triple junctions appeared tight and melt free at the resolution of the light microscope and the SEM. TEM analysis was limited and inconclusive, though some indications of grain boundary glass at triple junctions were observed. It is our overall interpretation of the combined observations that *most* of the in situ grain boundaries and triple junctions characterizing the samples during equilibration were tight and melt free.

Assuming that the ITM indeed is dominated by tight melt-free grain boundaries, we look to the published literature to assign a particular width and character to the grain boundaries, where some controversy has surrounded the topic. Observations and theory from ceramics, metals and some geological samples show that grain boundaries in most materials are free of an amorphous layer and, in silicates, have a structural width <1 nm (e.g., Ricoult and Kohlstedt, 1983; Yan et al., 1998; Hiraga et al., 1999; Schweinfest et al., 2004). For example, from Hiraga et al.

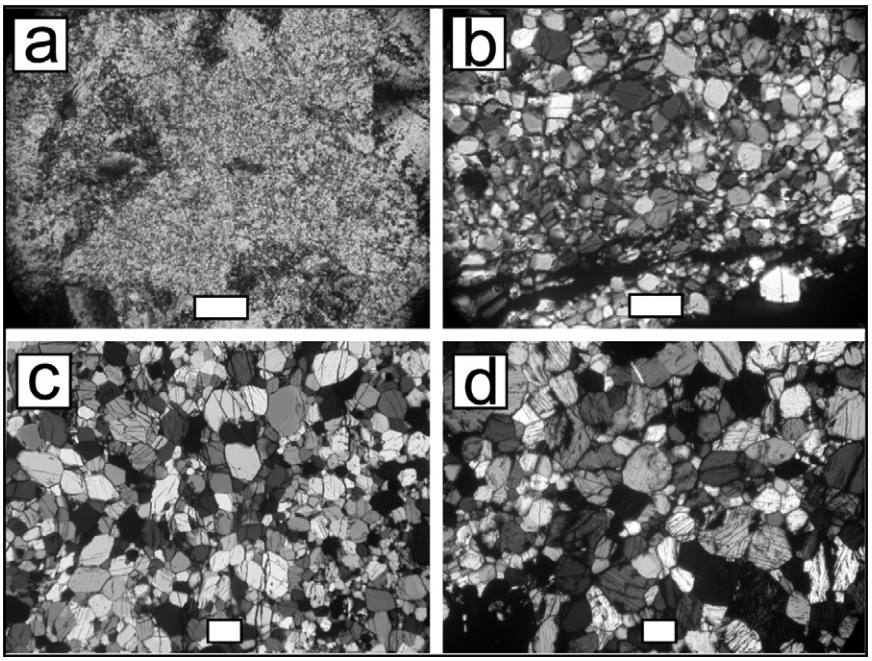

Fig. 7. Thin sections in cross-polarized light (gray scale images). 100 μm scale bar is shown at bottom in all four figures. Note change of scale between (a), (b) and (c), (d) and the amount of coarsening. (a) Sample EB040 (8 h). (b) Sample EB037 (20 h). (c) Sample EB036 (70 h). (d) Sample EB050 (180 h). Completely black areas in images represent either extinct grains or, in the bottom corners of (a) and (b), places where the thin section has been inadvertently polished away.

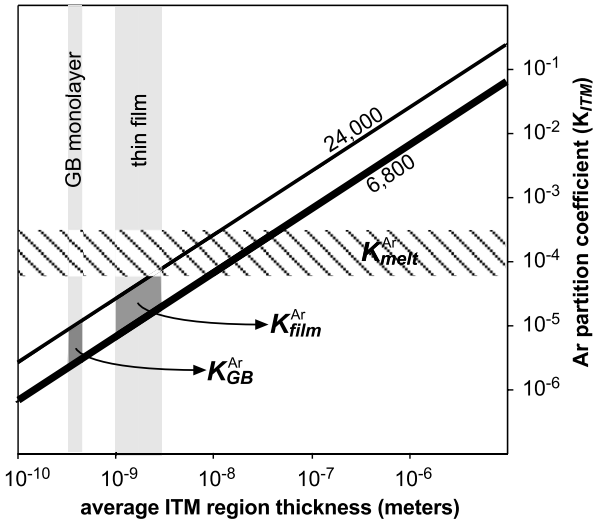

Fig. 8. Calculation of various K^{Ar}_{ITM} from $\overline{K}^{Ar}_{ITM}$ and assumed ITM thickness. Vertical bands show range of grain boundary thicknesses reported in the literature. Horizontal band shows K^{Ar}_{melt} determined by Chamorro et al. (2002). Diagonal lines of constant $\overline{K}^{Ar}_{ITM}$ determined in this study are shown. For dry grain boundary width (0.38 nm), K^{Ar}_{GB} for Ar is about a factor of 50 smaller than K^{Ar}_{melt}.

(2004), we calculate the structural grain boundary (monolayer) thickness in clinopyroxene aggregates such as ours to be 0.38 nm. However, the electro-chemical effects of grain boundaries in some materials could penetrate deeper, perhaps several 10s of nm, into the neighboring lattice due to space charge effects (e.g., Yan et al., 1983; Kingery, 1984). Finally, observations of geological samples by Farver and Yund (1995), Wirth (1996), Drury and Fitzgerald (1996), de Kloe et al. (2000) have indicated an effective grain boundary width of 1–5 nm, which has been referred to as a "thin film" of melt or amorphous material by some authors. Hiraga et al. (2002) dispute the "thin film" interpretation in mantle assemblages and discuss this controversy at length. Whether the ITM in our experimental samples was closer to a 1–5 nm "thin film" or to a 0.38 nm grain boundary is not possible to discern from our direct observations.

5.5.1. The possibility of micro-bubbles within the ITM

As discussed above, we interpret the significant release of gas upon capsule piercing as that gas residing in free gas bubbles within the capsule. The amount of gas released during pierce from bubbles is, not surprisingly, random and does not scale with grain size or grain boundary surface area. A separate question is whether or not we can rule out bubbles as contributing significantly to the higher temperature gas release that we do interpret as "GB" gas, or if most/all of the bubble gas is indeed released upon pierce. Two arguments support our interpretation that gas bubbles do not contribute significantly to the "GB" gas. First, the systematic relationship of decreasing GB argon with decreasing GB surface area is not consistent with the presence of bubbles. The amount or volume of total gas bubbles in the capsule will be independent of the grain size or grain boundary surface area. Changing grain size may affect how the bubbles are distributed within the sample, but not their total volume. Probably, the total volume of

gas bubbles in each experiment is a function of how well the capsule was evacuated, how much air was trapped in the capsule before welding, and how much gas was dissolved in the starting glass. Therefore, if anything, we would expect this amount to be random. Second, we have repeated a well-equilibrated 70 h run three times, each time reproducing the same relative amount of GB argon. Again, were this GB argon dominated by gas bubbles we would expect different, random amounts of bubble Ar in these three experiments. The reproducibility of the three 70 h runs, coupled with the systematic relationship of GB argon to grain size suggests that argon stored within the interconnected network of tight planar grain boundaries and their intersections, not bubbles, dominates the GB reservoir.

Even if bubbles and/or melt in the ITM affect to some extent the total amount of gas in the GB reservoir (and we acknowledge that they may be secondary factors), the quantification of partitioning between crystals and the ITM that surrounds them (i.e., $\overline{K}^{i}_{\mathrm{ITM}}$) are robust and, importantly, scalable with grain size. At worst, the persistence of minor bubbles after the pierce or the presence of melt would imply that the K^{i}_{GB} values (see Section 5.6) suggested in this paper are minimum values. Thus, while we are confident in our calculated values of $\overline{K}^{i}_{\mathrm{ITM}}$, we agree that the leap from $\overline{K}^{i}_{\mathrm{ITM}}$ to a true K^{i}_{ITM} includes unavoidable interpretive uncertainty regarding the exact nature of the ITM in our experiments, and in nature.

5.5.2. Comparison to an Ar monolayer

As discussed in Section 1.1, grain boundary partitioning has been described as the incorporation of impurities into a monolayer (that is, a sheet of the host phase one unit cell thick) of fixed maximum site occupancy. Hiraga et al. (2004) describe partitioning of Ca into the M2 sites of a clinopyroxene (or olivine) monolayer. Because an uncharged atom of Ar has a similar radius to a charged Ca^{2+} cation (both about 0.1 nm) it is reasonable to assume that GB Ar would also reside in the same sites as Ca^{2+}, perhaps charge-compensated by an O^{2-} vacancy.

If indeed the ITM Ar in our samples is confined to such a grain boundary monolayer, the total amount of GB Ar must not exceed this maximum occupancy. From the volume concentration (N_{M}) of these sites in clinopyroxene reported by Hiraga et al. (2004), we can calculate the maximum occupancy of Ar if it filled all grain boundary M-sites: $(N_{\mathrm{M}})^{2/3} = 6.9 \times 10^{14}$ M2-sites/cm^2 of GB. Because most of the Ar in our samples is in fact ^{40}Ar, we calculate the amount of ^{40}Ar within the inferred GB of each sample and compare it to the maximum occupancy above. We take the ^{40}Ar released at the "fuse" step to represent the true grain interior ^{40}Ar content. Converting to atomic units and dividing by the $\overline{K}^{\mathrm{Ar}}_{\mathrm{ITM}}$ (determined from the ^{37}Ar release pattern) we find that the occupancy of Ar per grain boundary area of all samples is at least three orders of magnitude below the maximum (see Table 5). These calculations confirm that Ar is a dilute trace element in these experiments and, even though it may be very strongly partitioned to the grain boundaries, the total amount is nowhere near the total occupancy limit represented by a monolayer of Ar-substituted clinopyroxene. All of the GB Ar could be easily accounted for by partitioning solely into tight 0.38 nm thick GB monolayers.

Table 5
Ar Monolayer calculations

Sample	Atoms ^{40}Ar/cm^2 of GB	Number of monolayers
EB028	6.21×10^{10}	8.94×10^{-5}
EB029	2.93×10^{11}	4.20×10^{-4}
EB030	4.54×10^{10}	6.53×10^{-5}
EB031	3.50×10^{10}	5.04×10^{-5}
EB033	2.63×10^{10}	3.79×10^{-5}
EB034	3.86×10^{10}	5.56×10^{-5}
EB035	1.03×10^{11}	1.49×10^{-4}
EB036	4.64×10^{10}	6.68×10^{-5}
EB037	8.95×10^{10}	1.29×10^{-4}
EB038	4.24×10^{10}	6.10×10^{-5}
EB040	2.38×10^{11}	3.42×10^{-4}
EB044	1.36×10^{12}	1.93×10^{-3}
EB048	1.29×10^{12}	1.86×10^{-3}
EB049	6.46×10^{10}	9.31×10^{-5}
EB050	4.80×10^{10}	6.91×10^{-5}
EB052	2.67×10^{11}	3.85×10^{-4}
EB053	4.04×10^{9}	5.82×10^{-6}
$(N_{\mathrm{M}})^{2/3}$ [a]	6.94×10^{14}	1.00

[a] Areal concentration of M2 sites at GB (Hiraga et al., 2003, 2004).

5.6. Calculation and comparison of a true partition coefficient

Fig. 8 shows our observed $\overline{K}^{\mathrm{Ar}}_{\mathrm{ITM}}$ vs. calculated $K^{\mathrm{Ar}}_{\mathrm{ITM}}$ as a function of the assumed average ITM width and character. For comparison, Chamorro et al. (2002) have published a diopside/melt partition coefficient for Ar ($K^{\mathrm{Ar}}_{\mathrm{melt}}$) at temperatures similar to our experiments at higher pressures ($P = 2$–8 GPa). If we assume the ITM is characterized by tight, melt-free grain boundaries and assign a width of 0.38 nm, we calculate $K^{\mathrm{Ar}}_{\mathrm{ITM}} = K^{\mathrm{Ar}}_{\mathrm{GB}}$ of $\sim 10^{-5}$–10^{-6}. If we select a nominally melt-free grain boundary width of ~1–5 nm, we calculate $K^{\mathrm{Ar}}_{\mathrm{ITM}} = K^{\mathrm{Ar}}_{\mathrm{film}}$ about an order of magnitude higher. Notably, either of $K^{\mathrm{Ar}}_{\mathrm{GB}}$ or $K^{\mathrm{Ar}}_{\mathrm{film}}$ is smaller than $K^{\mathrm{Ar}}_{\mathrm{melt}}$ of Chamorro et al. (2002) by at least an order to magnitude. If a nominal grain boundary region thickness of 10 nm is chosen, then the resultant $K^{\mathrm{Ar}}_{\mathrm{ITM}}$ is equal to the $K^{\mathrm{Ar}}_{\mathrm{melt}}$ published by Chamorro et al. (2002). Or, if only 0.1% of the grain boundary surfaces (say, at grain triple junctions) had a thickness of ~1 μm, that too would be consistent with $K^{\mathrm{Ar}}_{\mathrm{melt}}$ of Chamorro et al. (2002). Because of the uncertainty in the true nature of the ITM, each of these possibilities exists, though we favor the grain boundary scenario as discussed in Section 5.5. In this scenario, our results combined with those of Chamorro et al. (2002) yield a grain boundary/melt partition coefficient of about 50 (i.e., 50 times stronger preference for Ar in grain boundaries versus the melt). This suggests that noble gases prefer the grain boundary region strongly relative to incor-

poration into an ordered crystal structure and somewhat relative to the melt structure. If this is the case, then the Ar in the GB may be participating in a stabilizing (i.e., free energy lowering) structural transformation of the grain boundary (e.g., Yan et al., 1998).

6. Interpretations

It should be emphasized that while the calculations of K^i_{GB} from our data includes the uncertainty associated with the ITM characteristics and grain boundary thickness constraints discussed above, the measured values of $\overline{K}^i_{ITM}$ are well constrained. Ultimately, if the characteristics of the ITM in our experiments are similar to the characteristics of ITM in similar natural conditions (i.e., similar P–T, near zero volatile content), then the $\overline{K}^{Ar}_{ITM}$ and $\overline{K}^{He}_{ITM}$ parameters may be applied directly to comparable natural environments. It is reasonable to assume that the grain boundaries during our run were similar to pyroxene–pyroxene grain boundaries in similar melt-free mantle conditions, and perhaps similar to grain or phase boundaries involving more varied mineralogy.

6.1. Noble gas storage and transport in the earth

Using the values of $\overline{K}^{Ar}_{ITM}$ from this study we can predict [from R^{Ar}_{GB}; Eq. (1)] the bulk fraction of a rock's noble gas budget that would be stored at equilibrium in the grain boundary reservoir. Fig. 9 shows this relationship, which is strongly grain size dependent. For larger grain sizes ($d = 1$ cm) only 1–4% of the rock's Ar would be located in the grain boundaries. But for smaller grain size ($d = 1$ mm) the grain boundaries would hold up to 30% of the Ar budget. Dry grain boundaries, therefore, can represent a significant though not infinite reservoir of noble gases in the deep crust and mantle where no fluid phase is present, especially where grain size is small. However, when even a small melt fraction exists in the rock (for example, as little as 0.01% melt), the melt will begin to dominate the noble gas budget where all three "phases" (i.e., crystals, melt, and dry grain boundaries) are present together. If the melt fraction is increased to 0.1%, only a few percent of the total Ar budget is contained within grain boundaries. The distribution of Ar between these phases in an equilibrium closed system is shown as a function of melt fraction in Fig. 10. This figure shows the simplified case of a completely non-wetting melt phase among 1 mm grains, and thus represents an upper bound on the amount that could be stored in non-wetted grain boundaries. When interconnected fluids are present at melt fractions >0.1%, the storage and transport (by diffusion or advection) of noble gases will be dominated by the fluid. The grain boundary reservoir is only significant in very dry systems where the fluid phase present does not wet (and replace) planar grain boundaries. Nevertheless, a non-wetting melt of very low melt fraction (<0.1%) is *not* capable of extracting 100% of the noble gases out of fine grained mantle; some residual gas is retained by the grain boundaries (Fig. 10). This could potentially be significant in portions of the mantle where incipient melting begins and low carbonate or silicate melt fractions may exist (e.g., Dasgupta and Hirschmann, 2006).

Fig. 9 also shows that *bulk* noble gas storage in the dry mantle is a function of grain size. Assuming an equilibrium concentration of noble gas within crystal interiors, a given

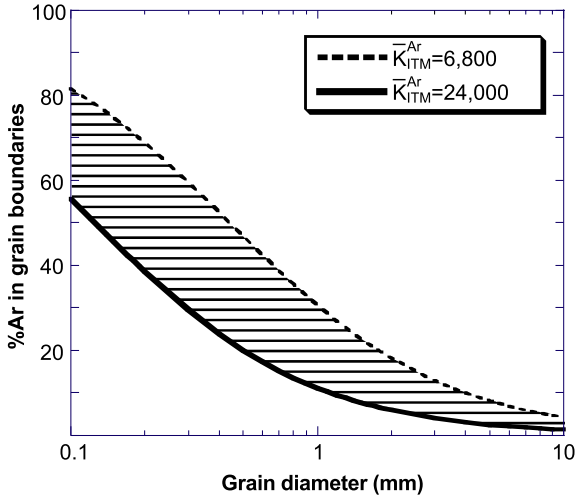

Fig. 9. Ar budget in a closed, dry mono-mineralic aggregate rock. In this scenario, only two reservoirs are available: crystal interiors and dry grain boundaries. Plotted are lines indicating the percent of the total argon in the rock located within the grain boundaries. Lines are calculated based on $\overline{K}^{Ar}_{ITM}$ determined in this study and Eq. (1). At finer grain sizes, grain boundaries represent a significant reservoir of the noble gases in a closed system at equilibrium.

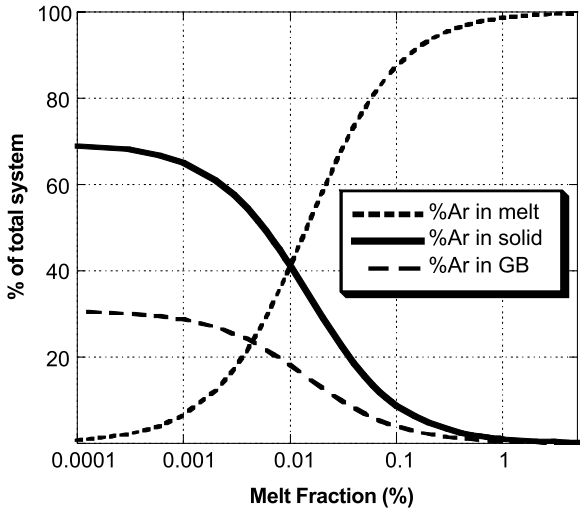

Fig. 10. Ar budget in a closed mono-mineralic system with variable melt content. In this scenario, three reservoirs are available: crystal interiors, grain boundaries, and melt. This figure is for a constant grain diameter of 1 mm and $\overline{K}^{Ar}_{ITM} = 6800\ m^{-1}$. At dry conditions (no melt), grain boundaries and crystals split the Argon as in Fig. 9. As melt fraction increases even to very low levels, melt begins to dominate the noble gas budget. This figure assumes completely non-wetting melt, an assumption which surely breaks down as melt fraction increases. The grain boundary fraction indicated here is therefore an upper bound at the higher melt fractions.

volume of mantle with smaller average grain sizes will store *in bulk* much more noble gas than an equal volume of coarse grained mantle. Portions of the crust or mantle which undergo localized, rapid deformation by diffusion creep may evolve such small grain sizes (e.g., Yamasaki, 2004), and therefore become important sinks or sponges for noble gases. When such fine-grained reservoirs are tapped by igneous processes, the result will be a much larger efflux of noble gases.

6.2. Geochronology and excess Ar or He in dry systems

Values of $\overline{K}^{Ar}_{ITM}$ may be used with the transmissive timescale (τ_T; Eq. 6) and the TLSC (Eq. 7) to predict the amount of internally derived excess Ar within a given mineral in a dry system. If dry grain boundaries were truly infinite sinks for noble gases, then radiogenic Ar would diffuse out of all minerals and excess Ar (in the minerals) would be limited in all situations. This is not the case. As described above, grain boundaries become unimportant once the fluid fraction increases beyond ~0.1%. But in dry systems, the grain boundaries represent the only non-mineral reservoir for radiogenic Ar and He. Fig. 9 shows that even for the fine grained systems, the grain boundaries cannot hold all of the noble gases. Therefore, in dry systems some radiogenic Ar and He will accumulate in minerals *above* their closure temperatures. Kelley and Wartho (2000) measured billions of years worth of excess Ar housed within mantle phlogopite where it had resided well above its closure temperature. In this setting, no melt phase was present (i.e., low TLSC) and Ar could not escape from the system (i.e., long τ_T), so the radiogenic ^{40}Ar accumulated mostly in minerals and dry grain boundaries.

The concentration of excess Ar accumulating in minerals can increase significantly with increasing grain size, particularly in dry systems. The following equation (from Baxter, 2003; note the minus sign before the 5/2 factor was inadvertently omitted from that published in Baxter, 2003) permits calculation of the amount of internally derived excess Ar in a given mineral within a system at a distance, L, from some effective external noble gas sink:

$$^{40}\mathrm{Ar}_{\text{excess-age-equivalent}}(L,t) \cong \frac{\tau_T^{Ar}}{2}\left(1-\exp\left(-5/2\cdot\frac{t}{\tau_T^{Ar}(1+\mathrm{TLSC}^{Ar})}\right)\right) \quad (8)$$

Note the dependency of excess Ar on τ_T and TLSC, both of which depend on $\overline{K}^{Ar}_{ITM}$. Because we lack an obvious constraint on D^{Ar}_{GB} and L, let us take the diffusivity of Ar in tholeiitic melt at 1350 °C (Lux, 1987) for D^{Ar}_{GB} and set $L = 1000$ m (for example; a 1000 m half-spacing of high diffusivity shear Zones) to illustrate the relative effects of grain size using Eq. (7). Fig. 11 shows that minerals in coarser grained systems (in systems that have evolved for the same time duration) house more Ar (and, hence, more excess radiogenic Ar) than finer grained equivalents where more of the excess Ar is partitioned into the more abundant grain boundaries. This factor is typically overlooked in thermochronology—the data presented here permit quantification of this important effect in dry systems.

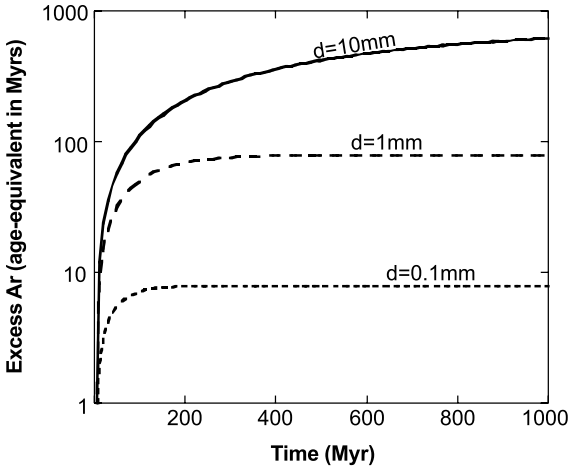

Fig. 11. Evolution of internally derived excess Ar in K-bearing minerals of a mono-mineralic uniform grain size system. Use of Eq. (8) assumes zero radiogenic ^{40}Ar in the rock at time = 0. For these calculations, $L = 1000$ m, $D^{Ar}_{GB} = 2\times10^{-2}$ m^2/yr (Lux, 1987), tortuosity (τ) = 0.7, $\overline{K}^{Ar}_{ITM} = 6800$ m^{-1}. τ_T and TLSC are calculated from these values using Eqs. (4)–(7) for a range of grain sizes. Excess Ar is plotted versus time of system evolution for three grain sizes: 10, 1, and 0.1 mm diameter. Once reached, steady state levels of excess Ar are much greater in coarse grained systems. Use of Eq. (8) applies only to systems at local noble gas equilibrium (i.e., when the minerals are well *above* their "closure" temperature).

7. Conclusions

The extent to which dry grain boundaries may act as a significant reservoir and/or bulk transport pathway for noble gases depends on the equilibrium partitioning between minerals and grain boundaries. The results of this study suggest that the intergranular region (ITM) in nominally dry polycrystalline diopside aggregates is dominated by tight grain boundaries which partition noble gases strongly over crystals. The grain-size-scaling $\overline{K}^{Ar}_{ITM}$ and $\overline{K}^{He}_{ITM}$ parameters constrained by our experiments should be applied directly to comparable natural conditions in dry portions of the mantle and deep crust. Dry grain boundaries may retain a significant proportion of the bulk noble gas budget of a rock if the following conditions hold—(1) grain size is relatively small (i.e., <1 mm), (2) there is very little melt or aqueous fluid present. In coarse grained ($\sim d > 1$ cm) and/or fluid bearing systems, dry grain boundaries are insignificant reservoirs. Bulk transport out of drier and/or coarser grained systems will be relatively slow resulting in the accumulation of significant radiogenic Ar and He in local minerals at equilibrium.

Acknowledgments

This study was conducted at Caltech. Manuscript preparation was conducted while EFB was at Boston University. We Jed Mosenfelder, John Beckett and Mike Baker for

help with the experiments. We thank Pete Burnard for assistance with the noble gas analysis. We thank Carol Garland for TEM preparation and analysis. Steve Reese of the OSU Reactor Facility was helpful in accommodating our irradiations. We thank Lauren Cooper and Jennifer Wade for assistance in thin section observation. Ed Stolper provided the starting material and access to his labs. We thank Bruce Watson, Takeo Hiraga, and Terry Plank for valuable discussions at various stages of the project. Support from a Caltech Postdoctoral Fellowship to EFB and NSF Grants EAR-0125784 (to PDA and KAF) and EAR-0337527 (to EFB) is gratefully acknowledged.

Associate Editor: Jun-ichi Matsuda

Appendix A. Supplementary data

Supplementary data associated with this article can be found, in the online version, at doi:10.1016/j.gca.2006.09.011.

References

Allegre, C.J., Staudacher, T., Sarda, P., 1986. Rare gas systematics: formation of the atmosphere, evolution and structure of the Earth's mantle. *Earth Planet. Sci. Lett.* **81**, 127–150.

Baxter, E.F., 2003. Quantification of the factors controlling the presence of excess ^{40}Ar or ^{4}He. *Earth Planet. Sci. Lett.* **216**, 619–634.

Baxter, E.F., DePaolo, D.J., 2002. Field measurement of high temperature bulk metamorphic reaction rates I: theory and technique. *Am. J. Sci.* **302**, 442–464.

Baxter, E.F., DePaolo, D.J., Renne, P.R., 2002. Spatially correlated anomalous 40Ar/39Ar "age" variations in biotites about a lithologic contact near Simplon Pass, Switzerland: a mechanistic explanation for excess Ar. *Geochim. Cosmochim. Acta* **66**, 1067–1083.

Brady, J.B., 1983. Intergranular diffusion in metamorphic rocks. *Am. J. Sci.* **283A**, 181–200.

Broadhurst, C.L., Drake, M.J., Hagee, B.E., Bernatowicz, T.J., 1990. Solubility and partitioning of Ar in anorthite, diopside, forsterite, spinel, and synthetic basaltic liquids. *Geochim. Cosmochim. Acta* **54**, 299–309.

Broadhurst, C.L., Drake, M.J., Hagee, B.E., Bernatowicz, T.J., 1992. Solubility and partitioning of Ne, Ar, Kr, and Xe in minerals and synthetic basaltic melts. *Geochim. Cosmochim. Acta* **56**, 709–723.

Brooker, R.A., Wartho, J-A., Carroll, M.R., Kelley, S.P., Draper, D.S., 1998. Preliminary UVLAMP determinations of argon partition coefficients for olivine and clinopyroxene grown from silicate melts. *Chem. Geol.* **147**, 185–200.

Brooker, R.A., Du., Z., Blundy, J.D., Kelley, S.P., Allan, N.L., Wood, B.J., Chamorro, E.M., Wartho, J.-A., Purton, J.A., 2003. The 'zero-charge' partitioning behavior of noble gases during mantle melting. *Nature* **423**, 738–741.

Carroll, M.R., Stolper, E.M., 1993. Noble gas solubilities in silicate melts and glasses: new experimental results for Ar and the relationship between solubility and ionic porosity. *Geochim. Cosmochim. Acta* **57**, 5039–5051.

Carroll, M.R., Draper, D.S., Brooker, R.A., Kelley, S.P., 1994. Noble gas solubilities in melts and crystals. In: Matsuda, J.I. (Ed.), *Noble Gas Geochemistry and Cosmochemistry*. Terra Scientific Publications, pp. 325–341.

Chamorro, E.M., Brooker, R.A., Wartho, J.-A., Wood, B.J., Kelley, S.P., Blundy, J.D., 2002. Ar and K partitioning between clinopyroxene and silicate melt to 8 GPa. *Geochim. Cosmochim. Acta* **66**, 507–519.

Culler, T.S., Becker, T.A., Muller, R.A., Rene, P.R., 2000. Lunar impact history from ^{40}Ar/^{39}Ar dating of glass spherules. *Science* **287**, 1785–1788.

Dasgupta, R., Hirschmann, M.M., 2006. Melting in the Earth's deep upper mantle caused by carbon dioxide. *Nature* **440**, 659–662.

de Kloe, R., Drury, M.R., van Roermund, H.L.M., 2000. Evidence for stable grain boundary melt films in experimentally deformed olivine-orthopyroxene rocks. *Phys. Chem. Mineral.* **27**, 480–494.

Drury, M.R., Fitzgerald, J.D., 1996. Grain boundary melt films in an experimentally deformed olivine-orthopyroxene rock: implications for melt distribution in upper mantle rocks. *Geophys. Res. Lett.* **23**, 701–704.

Dunai, T.J., Porcelli, D., 2002. Storage and transport of noble gases in the subcontinental lithosphere. *Rev. Min. Geochem.* **47**, 371–409.

Farley, K.A., 2002. (U–Th)/He dating: techniques, calibrations, and applications. *Rev. Mineral. Geochem.* **47**, 819–844.

Farver, J.R., Yund, R.A., 1995. Grain boundary diffusion of oxygen, potassium and calcium in natural and hot pressed feldspar aggregates. *Contrib. Mineral. Petrol.* **118**, 340–355.

Fechtig, H., Gentner, W., Zahringer, J., 1960. Argonbestimmungen an Kaliummineralien-VII Diffusionsvertuste von argon in mineralien und ihre auswirkung auf die kalium-argon-altersbestimmung. *Geochim. Cosmochim. Acta* **19**, 70–79.

Fechtig, H., Gentner, W., Kalbitzer, S., 1961. Argonbestimmungen an Kaliummineralien-IX Messungen zu den verschiedenen arten der argondiffusion. *Geochim. Cosmochim. Acta* **25**, 297–311.

Foland, K.A., 1979. Limited mobility of argon in a metamorphic terrain. *Geochim. Cosmochim. Acta* **43**, 793–801.

Hess, P.C., 1994. Thermodynamics of thin films. *J. Geophys. Res.* **99**, 7219–7229.

Hiraga, T., Nagase, T., Akizuki, M., 1999. The structure of grain boundaries in granite-origin ultramylonite studied by high-resolution electron microscopy. *Phys. Chem. Mineral.* **26**, 617–623.

Hiraga, T., Anderson, I.M., Zimmerman, M.E., Mei, S., Kohlstedt, D.L., 2002. Structure and chemistry of grain boundaries in deformed, olivine + basalt and partially molten lherzolite aggregates: evidence of melt-free grain boundaries. *Contrib. Mineral. Pet.* **144**, 163–175.

Hiraga, T., Anderson, I.M., Kohlstedt, D.L., 2003. Chemistry of grain boundaries in mantle rocks. *Am. Min.* **88**, 1015–1019.

Hiraga, T., Anderson, I.M., Kohlstedt, D.L., 2004. Grain boundaries as reservoirs of incompatible elements in the Earth's mantle. *Nature* **427**, 699–703.

Hiyagon, H., Ozima, M., 1986. Partition of noble gases between olivine and basalt melt. *Geochim. Cosmochim. Acta* **50**, 2045–2057.

Kelley, S.P., 2002a. Excess argon in K–Ar and Ar–Ar geochronology. *Chem. Geol.* **188**, 1–22.

Kelley, S.P., 2002b. K–Ar and Ar–Ar dating. *Rev. Min. Geochem.* **47**, 785–818.

Kelley, S.P., Wartho, J-A., 2000. Rapid kimberlite ascent and the significance of Ar–Ar ages in xenolith phlogopites. *Science* **289**, 609–611.

Kingery, W.D., 1984. Segregation phenomena at surfaces and at grain boundaries in oxides and carbides. *Solid State Ionics* **12**, 299–307.

Lange, R.A., Deyoreo, J.J., Navrotsky, A., 1991. Scanning calorimetric measurement oh heat-capacity during incongruent melting of diopside. *Amer. Min.* **76**, 904–912.

Lux, G., 1987. The behavior of noble gases in silicate liquids: Solution, diffusion, bubbes, and surface effects, with application to natural samples. *Geochim. Cosmochim. Acta* **51**, 1549–1560.

McDougall, I., Harrison, T.M., 1999. *Geochronology and Thermochonology by the ^{40}Ar/^{39}Ar Method*. Oxford University Press, New York.

McLean, D., 1957. *Grain Boundaries in Metals*. Clarendon Press, Oxford.

Mendelson, M.I., 1969. Average grain size in polycrystalline ceramics. *J. Am. Ceramic Soc.* **52**, 443–446.

Ozima, M., Podosek, F.A., 2002. *Noble Gas Geochemistry*, second ed. Cambridge Univesity Press, New York.

Parman, S.W., Kurz, M.D., Hart, S.R., Grove, T.L., 2006. Helium solubility in olivine and implications for high ^{3}He/^{4}He in ocean island basalts. *Nature* **437**, 1140–1143.

Porcelli, D., Wasserburg, G.J., 1995. Mass transfer of helium, neon, argon, and xenon through a steady-state upper mantle. *Geochim. Cosmochim. Acta* **59**, 4921–4937.

Porcelli, D., Ballentine, C.J., Wieler, R. (Eds.), 2002. *Noble Gases in Geochemistry and Cosmochemistry*. Mineralogical Society of America, Washington.

Renne, P.R., 2000. $^{40}Ar/^{39}Ar$ age of plagioclase from Acapulco meteorite and the problem of systematic errors in cosmochronology. *Earth Planet. Sci. Lett.* **175**, 13–26.

Renne, P.R., Norman, E.B., 2001. Determination of the half-life of ^{37}Ar by mass spectrometry. *Phys. Rev. C* **63**, 047302.

Ricoult, D.L., Kohlstedt, D.L., 1983. Structural width of low-angle grain boundaries in olivine. *Phys. Chem. Mineral.* **9**, 133–138.

Roselieb, K., Blanc, P., Buttner, H., Jambon, A., Rammensee, W., Rosenhauer, M., Vielzeuf, D., Walter, H., 1997. Experimental study of argon sorption in quartz: evidence for argon incompatibility. *Geochim. Cosmochim. Acta* **61**, 533–542.

Rutter, E.H., 1976. The kinetics of rock deformation by pressure solution. *Philos. Trans. R Soc. Lond.* **A283**, 203–219.

Rutter, E.H., 1983. Pressure solution in nature, theory and experiment. *J. Geol. Soc. Lond.* **140**, 725–740.

Scaillet, S., 1996. Excess ^{40}Ar transport scale and mechanism in high-pressure phengites: a case study from an eclogitized metabasite of the Dora-Maira nappe, western Alps. *Geochim. Cosmichim. Acta* **60**, 1075–1090.

Schweinfest, R., Paxton, A.T., Finnis, M.W., 2004. Bismuth embrittlement of copper is an atomic size effect. *Nature* **432**, 1008–1011.

Shuster, D.L., Farley, K.A., 2005. Diffusion kinetics of proton induced Ne-21, He-3, and He-4 in quartz. *Geochim. Cosmochim. Acta* **69**, 2349–2359.

Shuster, D.L., Vasconcelos, P.M., Heim, J.A., Farley, K.A., 2005. Weathering geochronology by (U–Th)/He dating of goethite. *Geochim. Cosmochim. Acta* **69**, 659–673.

Smith, C.S., Guttman, L., 1953. Measurement of internal boundaries in three-dimensional structures by random sectioning. *Trans. AIME* **197**, 81–86.

Sutton, A.P., Balluffi, R.W., 1995. *Interfaces in Crystalline Materials*. Clarendon Press, Oxford.

Turner, G., 1970. Argon-40/argon-39 dating of lunar rock samples. *Science* **167**, 466–468.

Vasconcelos, P.M., Renne, P.R., Brimhall, G.H., Becker, T.A., 1994. Direct dating of weathering phenomena by $^{40}Ar/^{39}Ar$ and K–Ar analysis of supergene K–Mn oxides. *Geochim. Cosmochim. Acta* **58**, 1635–1665.

Watson, E.B., Cherniak, D.J., 2003. Lattice diffusion of Ar in quartz wit hconstraints on Ar solubility and evidence of nanopores. *Geochim. Cosmochim. Acta* **67**, 2043–2062.

Wirth, R., 1996. Thin amorphous films (1–2 nm) at olivine grain boundaries in mantle xenoliths from San Carlos, Arizona. *Contrib. Mineral. Pet.* **124**, 44–54.

Yamasaki, T., 2004. Localized rheological weakening by grain-size reduction during lithospheric extension. *Tectonophysics* **386**, 117–145.

Yan, M.F., Cannon, R.M., Bowen, H.K., 1983. Space charge, elastic field, and dipole contributions to equilibrium solute segregation at interfaces. *J. Appl. Phys.* **54**, 764–778.

Yan, Y., Chisholm, M.F., Duscher, G., Maiti, A., Pennycook, S.J., Pantelides, S.T., 1998. Impurity-induced structural transformation of a MgO grain boundary. *Phys. Rev. Lett.* **81**, 3675–3678.